Rattle-Type Fe_3O_4@CuS Developed to Conduct Magnetically Guided Photoinduced Hyperthermia at First and Second NIR Biological Windows

*Ze-Cong Wu, Wei-Peng Li, Cheng-Hung Luo, Chia-Hao Su, and Chen-Sheng Yeh**

A therapeutic carrier in the second near-infrared (NIR) window is created that features magnetic target, magnetic resonance imaging (MRI) diagnosis, and photothermal therapy functions through the manipulation of a magnet and NIR laser. A covellite-based CuS in the form of rattle-type Fe_3O_4@CuS nanoparticles is developed to conduct photoinduced hyperthermia at 808 and 1064 nm of the first and second NIR windows, respectively. The Fe_3O_4@CuS nanoparticles exhibit broad NIR absorption from 700 to 1300 nm. The in vitro photothermal results show that the laser intensity obtained using 808 nm irradiation required a twofold increase in its magnitude to achieve the same damage in cells as that obtained using 1064 nm irradiation. Because of the favorable magnetic property of Fe_3O_4, magnetically guided photothermal tumor ablation is performed for assessing both laser exposures. According to the results under the fixed laser intensity and irradiation spot, exposure to 1064 nm completely removed tumors showing no signs of relapse. On the other hand, 808 nm irradiation leads to effective inhibition of growth that remained nearly unchanged for up to 30 d, but the tumors are not completely eliminated. In addition, MRI is performed to monitor rattle-type Fe_3O_4@CuS localization in the tumor following magnetic attraction.

1. Introduction

Materials absorbing radiation in the near-infrared (NIR) range are considered suitable agents for photothermal cancer therapy. In the past five years, photothermal nanoagents, such as copper sulfides, including covellite (CuS), and djurleite ($Cu_{2-x}S$), have gained considerable attention. This is because of their appreciable absorption in the NIR region, low cost of fabrication, and acceptable cytotoxicity. The *d*–*d* electronic transitions of Cu^{2+} has been suggested to account for the broad absorption in the NIR region for covellite CuS.[1] Nevertheless, the plasmonic property has also been recently given discussion that indicated the optical behavior depending on particle size and shape.[2] The origins of the NIR absorption bands of covellite (CuS) remains controversial. In any case, CuS exhibits broad and strong NIR absorption beyond 1000 nm. This is different from Au nanorods, of which the band is mainly located at 800 nm when the appropriate aspect ratio for Au rods is applied in vivo. Although CuS nanoparticles exhibit absorption around 800 nm, they potentially present a stronger photothermal therapeutic effect in the second NIR window (1000–1350 nm), whereas Au nanorods have a stronger effect in the first NIR window (650–950 nm). The length of an Au nanorod is usually prolonged to 300–600 nm, which is not suitable for in vivo studies, to make its longitudinal mode to appear in the second NIR biological region.[3] The second region (1000–1350 nm) is recognized to offer more efficient tissue penetration compared with the first region (650–950 nm) when absorption and scattering effects in a tissue are considered.[4] For example, hemoglobin has substantially low absorption in the NIR wavelengths, and blood is sufficiently transparent in the range 1000–1350 nm. The reported photothermal therapeutic CuS[5] has nearly been limited by use of 980 and 808 nm wavelengths for in vitro and in vivo irradiation. Water has a strong absorption band at 980 nm and thus is the most concentrated NIR absorber in biological tissues. Continuous exposure to 980 nm irradiation can substantially increase temperature, thus damaging cells and tissues.[6] No relevant information regarding the therapeutic effect of covellite CuS in the second NIR window is available. From the perspective of nanomaterial fabrication, previous studies have mainly focused on investigating nonhybrid and core–shell CuS nanoparticles.[5,7] The rattle-type hybrid CuS nanoparticles have yet to be formed. The introduction of an additional iron oxide ingredient would immediately endow CuS with magnetic properties and applications as well as a photothermal benefit.

We developed rattle-type Fe_3O_4@CuS NPs with delocalized Fe_3O_4 nanoparticles inside hollow porous CuS structures (**Scheme 1**). The rattle-type Fe_3O_4@CuS nanoparticles exhibited broad NIR absorption from 700 to 1300 nm. A greater absorption coefficient ($\varepsilon_{1064\ nm} = 4.9 \times 10^{10}\ cm^{-1}\ M^{-1}$) was obtained for 1064 nm irradiation than for 808 nm irradiation

Z.-C. Wu, Dr. W.-P. Li, Dr. C.-H. Luo, Prof. C.-S. Yeh
Department of Chemistry and Technology and
Advanced Optoelectronic Technology Center
National Cheng Kung University
Tainan 701, Taiwan
E-mail: csyeh@mail.ncku.edu.tw
Prof. C.-H. Su
Center for Translational Research in Biomedical Sciences
Kaohsiung Chang Gung Memorial Hospital
Kaohsiung 833, Taiwan

DOI: 10.1002/adfm.201503015

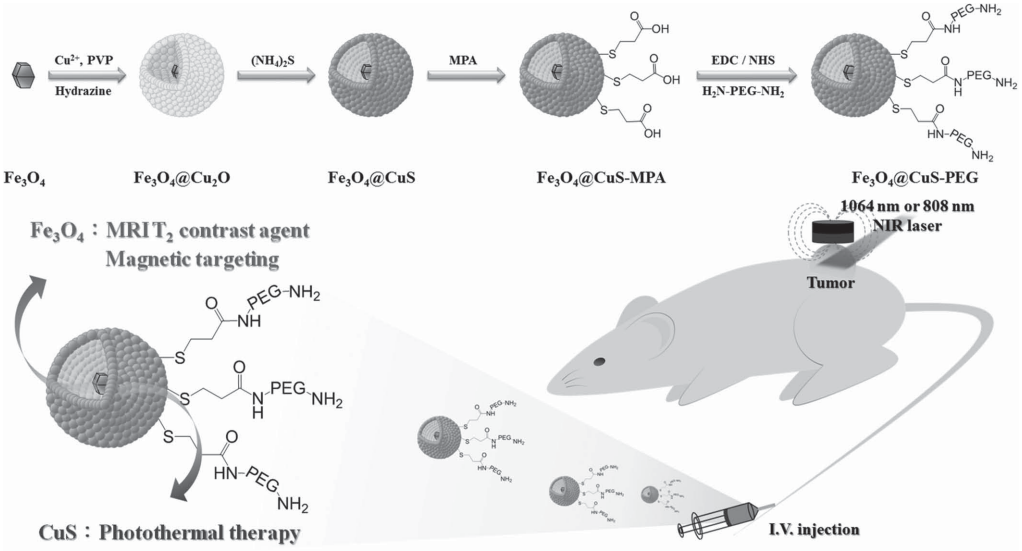

Scheme 1. Illustration of the synthetic processes of the Fe_3O_4@CuS-PEG NPs for in vivo tumor treatment by means of magnetic targeting and NIR radiation (1064 and 808 nm).

($\varepsilon_{808\ nm} = 3.5 \times 10^{10}\ cm^{-1}\ M^{-1}$). Thus, the laser intensity obtained using 808 nm irradiation required a twofold increase to achieve the same damage in cells as that obtained using 1064 nm irradiation. Because of the favorable magnetism of Fe_3O_4, magnetically guided photothermal tumor ablation conducted to assess 808 and 1064 nm laser exposure. According to the results under the fixed laser intensity and irradiation beam spot, irradiation exposure at 1064 nm completely removed the tumor and showed no signs of relapse. Using 808 nm irradiation led to effective inhibition of growth that remained almost unchanged for up to 30 d, but the tumor was not completely eliminated. In addition, magnetic resonance imaging (MRI) was performed to monitor rattle-type Fe_3O_4@CuS localization in the tumor following magnetic attraction after tail vein injection. From the nanomedicine research perspective, we created a therapeutic carrier in the second NIR window that features magnetic target, MRI diagnosis, and photothermal therapy functions through the manipulation of a magnet and NIR laser.

2. Results and Discussion

2.1. Preparation, Characterization, and Formation of Rattle-Type Fe_3O_4@CuS NPs

In this study, we synthesized iron oxide (Fe_3O_4) nanoparticles (NPs) from the precursors iron (III) acetylacetonate, trioctylamine, and oleic acid (OA) by using the thermal decomposition method presented in our previous report.[8] **Figure 1**a shows a transmission electron microscope (TEM) image of the OA-coated Fe_3O_4 NPs measuring (length between diagonal apices) 27.8 ± 1.9 nm. Figure S1 of the Supporting Information illustrates a high-resolution (HR)-TEM image of the Fe_3O_4 NPs, indicating that the Fe_3O_4 NPs exhibit a truncated morphology. The HR-TEM images obtained in the [110] and [001] directions reveal that the morphology of the synthesized Fe_3O_4 NPs is a truncated octahedron. The truncated octahedron in the [110] zone axis comprises eight {111} and six {001} planes.[8,9] The electron diffraction spectra indicated that the Fe_3O_4 NP is a single-crystal structure. Furthermore, the electron diffraction points were distributed in a square shape, indicating that the crystalline phase of the Fe_3O_4 particle is cubic phase (Figure S1d, Supporting Information).

Because the surface of the as-synthesized Fe_3O_4 particles was protected by OA (oleic acid), we used hexadecyltrimethylammonium bromide (CTAB) to convert oil-phase Fe_3O_4 NPs into aqueous-phase Fe_3O_4 through hydrophobic van der Waals interaction with OA long carbon chain interactions. The TEM image (Figure 1b) indicates that the original truncated octahedral morphology was not influenced by the aqueous phase conversion. The insets in Figure 1a,b show that Fe_3O_4 NPs dispersed in oil-phase n-hexane (the upper layer) and aqueous phase water (lower layer). The surface potential was measured using a particle size and interface potential analyzer (Dynamic Light Scattering, DLS). The resulting surface potential was +40.3 mV (Figure S2, Supporting Information), indicating the existence of positively charged CTAB for modification on the surface of iron oxide.

The method used for preparing rattle-type Fe_3O_4@CuS NPs involving core–shell Fe_3O_4@Cu_2O particles as sacrificial templates before replacing oxygen ions with sulfur ions through a modified Kirkendall process (Scheme 1).[10] The strategy for synthesizing Cu_2O particles entailed reducing copper ions (Cu^{2+}) to Cu_2O NPs by using strong reductant hydrazine, followed by gathering small Cu_2O NPs into large Cu_2O NPs through physical adsorption by using polyvinylpyrrolidone (PVP).[11] We used the property of Fe_3O_4@CTAB of having a positive charge on the surface because of the positive charge of the trimethylammonium ($N(CH_3)_3^+$) functional group on CTAB and of PVP of having a negative charge because of a polarizable carbonyl (C=O) group to facilitate an electrostatic interaction between them.[12] In addition, PVP was used to capture Cu_2O NPs for forming core–shell Fe_3O_4@Cu_2O NPs (Figure 1c). The TEM image reveals that the resulting Fe_3O_4@Cu_2O NPs exhibited a

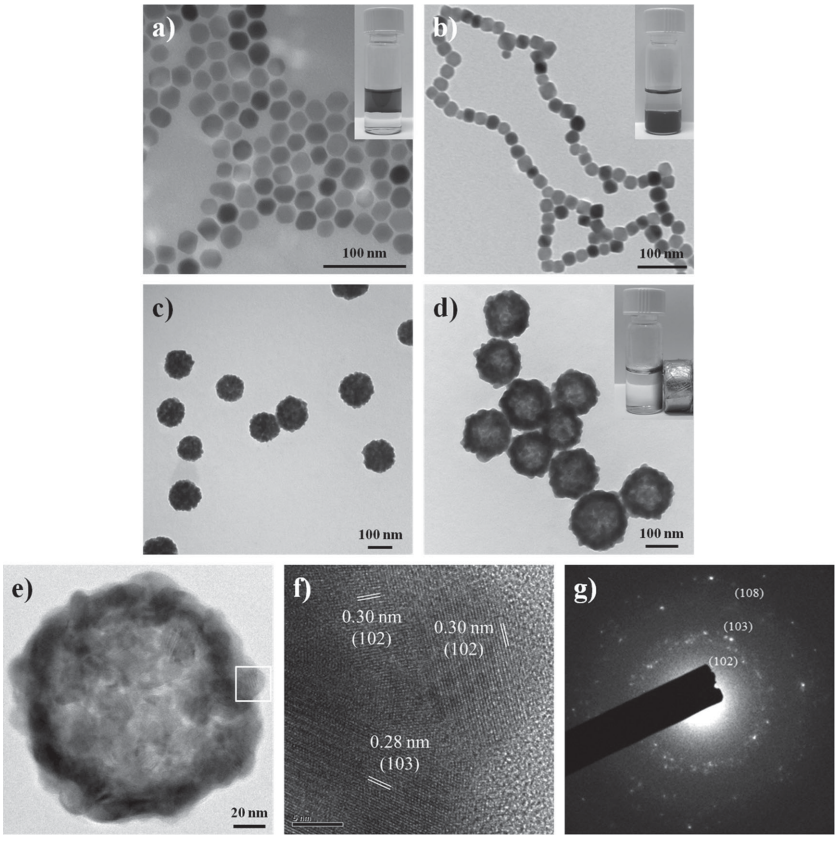

Figure 1. TEM images show both a) hydrophobic and b) hydrophilic Fe_3O_4 NPs; insets: Fe_3O_4 NPs dispersed in oil (top) or water phase (bottom). c) TEM image of Fe_3O_4@Cu_2O NPs. d) TEM image of Fe_3O_4@CuS NPs; inset: Fe_3O_4@CuS colloidal solutions attracted by an external magnet. e) HR-TEM image of a single Fe_3O_4@CuS NP. f) The magnified image of the CuS shell from the white marked area of (e). g) The electron diffraction pattern from the [010]-oriented Fe_3O_4@CuS NP.

spherical morphology. The size of the Fe_3O_4@Cu_2O NPs synthesized using this strategy was controllable. The particle size of Fe_3O_4@Cu_2O decreased as the total volume of the reaction solution increased (Figure S3, Supporting Information). On the other hand, Fe_3O_4@Cu_2O showed a smoother (smooth surface) and more integral circular morphology as its particle size increased. Considering the subsequent in vivo animal experiments, we used Fe_3O_4@Cu_2O with a particle size of 120 nm for further experiments.

Regarding the reaction mechanism underlying the conversion of solid Cu_2O into hollow CuS through the modified Kirkendall process, keeping Cu_2O in water or exposing it directly to air induces it to react with oxygen in the water or air and becomes oxidized into CuO; this is because Cu_2O is unstable at room temperature, as explained by Pang and Zeng.[10] Therefore, when the Cu_2O NPs were placed in water, their surfaces were oxidized to form a thin CuO lamella. When sulfur ions were added, the CuO lamella reacted with the added ions to form a CuS (copper sulfide) lamella. Moreover, such a thin CuS lamella was used as a substrate for the subsequent nucleation and growth of CuS. As the reaction time increased, the inner layer of Cu_2O was gradually oxidized to release copper ions, which were precipitated and eventually deposited on the outer CuS lamella to form hollow CuS NPs. Moreover, because Cu_2O has a higher solubility compared with CuO, Cu_2O was directly dissolved to form CuS as one of the possible reaction mechanism.

According to Pearson's hard and soft acid–base principle,[13] a soft base forms a stable complex with a soft acid, whereas a hard base forms a stable complex with a hard acid. Cuprous (Cu^+) and copper ions (Cu^{2+}) are soft acids, a sulfur ion is a soft base, and oxygen is a hard base; hence, the interaction of cuprous and copper ions with sulfur ions is stronger than their interaction with oxygen ions. Therefore, as Cu_2O NPs undergo a sulfurization reaction, a pure-phase CuS structure is available as long as sufficient sulfur ions are added to the reaction.[5d,10] In this synthesis strategy, $(NH_4)_2S$ (ammonium sulfide) was used as a source of sulfur ions to transform core–shell Fe_3O_4@Cu_2O NPs into rattle-type Fe_3O_4@CuS NPs, and the absorption of CuS was controlled by changing the dosage of $(NH_4)_2S$ (Figure S4, Supporting Information). Figure S4a of the Supporting Information shows that when $[(NH_4)_2S]/[Cu^{2+}] = 1$, the morphology of the CuS demonstrated a hollow structure, and as $[(NH_4)_2S]/[Cu^{2+}]$ was increased to 1.75, the morphology and size of the CuS NPs remained unchanged. The UV–vis–NIR spectra in Figure S4b of the Supporting Information indicates that the absorption of NIR increased with the dosage of $(NH_4)_2S$; however, the NIR absorption did not show an apparent increase when $[(NH_4)_2S]/[Cu^{2+}] = 1.5$–1.75. Therefore, we used $[(NH_4)_2S]/[Cu^{2+}] = 1.5$ for preparing the Fe_3O_4@CuS NPs. The TEM graph depicted in Figure 1d shows the morphology of the as-prepared Fe_3O_4@CuS NPs, indicating that the particle size of hollow CuS is approximately 139.3 nm and that its shell thickness is approximately 26.6 nm. Nevertheless, because the atomic weight of iron (55.8) is approximately similar to that of copper (63.5), no apparent contrast was observed on the TEM image; hence, the TEM image did not indicate a clear rattle structure. To confirm the existence of iron oxide in the synthesized Fe_3O_4@CuS NPs, we conducted a magnetic attraction for the colloidal solution by using a magnet (inset of Figure 1d). In addition, the proportion of copper and iron atoms in this material was quantified using an inductively coupled plasma-atomic emission spectrometer (ICP-AES). The results of this quantification indicated that the molar ratio of copper and iron atoms was 5.3:1.

Figure 1e illustrates the HR-TEM image of the Fe_3O_4@CuS NPs, and Figure 1f depicts a partially magnified section (corresponding to the red box) of this image, indicating that the CuS shell in the [010] zone axis direction has a (102) plane with a lattice spacing (*d*-spacing) of 0.30 nm and a (103) plane with a lattice spacing of 0.28 nm. Therefore, the synthesized CuS shell can be assigned to be a hexagonal phase.[5b] In

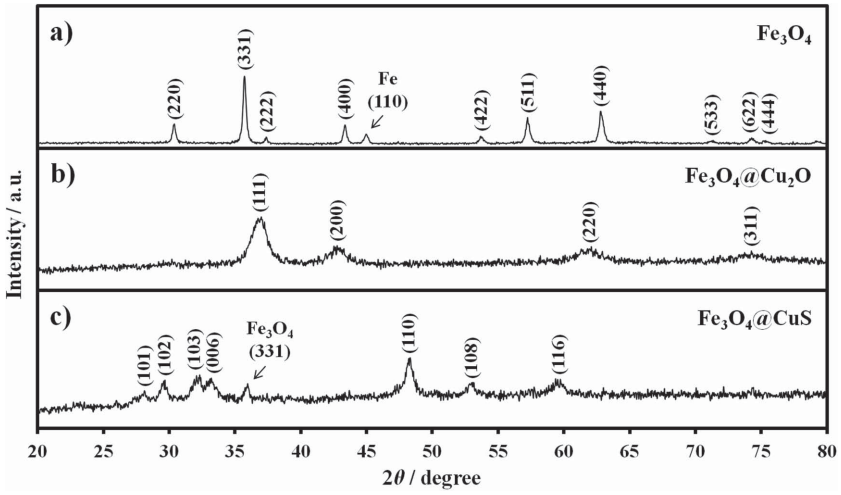

Figure 2. XRD patterns of a) Fe_3O_4 NPs, b) Fe_3O_4@Cu_2O NPs, and c) Fe_3O_4@CuS NPs using a Cu $K\alpha$ radiation ($\lambda = 1.5418$ Å) source.

addition, the crystal face on the CuS shell was not continuous that shown in Figure 1e, from which the SAED (selected area electron diffraction) spectrum in the [010] zone axis direction presented a polycrystal structure for the electron diffraction pattern (Figure 1g). **Figure 2** shows the X-ray diffraction (XRD) spectra of the Fe_3O_4 NPs, core–shell Fe_3O_4@Cu_2O, and rattle-type Fe_3O_4@CuS. The synthesized iron oxide exhibits a cubic inverse spinel structure (JCPDS card no. 19–0629) accompanied with a diffraction peak of iron (α-Fe) giving a (110) plane at a diffraction angle of 45° (Figure 2a). Figure 2b indicates that the cuprous oxide of the core–shell Fe_3O_4@Cu_2O NPs demonstrates a cubic phase (JCPDS card no. 05–0667). However, this XRD spectrum shows no Fe_3O_4 diffraction peak; this is probably because the surfaces of the Fe_3O_4 NPs were covered by a cuprous oxide with a thickness of approximately 46 nm. Figure 2c shows that the CuS shell of the rattle-type Fe_3O_4@CuS NPs exhibits a hexagonal phase covellite structure (JCPDS card no. 06–0464), and the diffraction peak of the Fe_3O_4 (331) plane reappears at a diffraction angle of 36°. Therefore, the Fe_3O_4 NPs were observed to coexist with a hollow CuS.

To prove that the Fe_3O_4@CuS NPs present a rattle-type structure, we conducted energy-dispersive X-ray spectroscopy (EDS) for assessing the structure of these NPs. **Figure 3**a–e shows composition mapping for the Fe_3O_4@CuS NPs. A higher density of copper and sulfur elements was observed around the periphery than at the center, and iron elements were mainly distributed internally; these observations indicated that Fe_3O_4 was enclosed in the hollow CuS. We also applied the EDS elemental analysis to different positions of this material (Figure S5, Supporting Information). The results revealed that the iron elements were located in the center of the material, whereas only copper and sulfur signals were observed in the shell. We further performed a line scan analysis for the Fe_3O_4@CuS NPs. We confirmed that Fe_3O_4 was in the interior, whereas the periphery was covered with hollow CuS (Figure 3f). In addition, the different particles were examined for the line scan analysis, indicating that Fe_3O_4 did not exist at a fixed position inside the hollow nanostructure, giving that Fe_3O_4@CuS NPs have a rattle-type structure (Figure S6, Supporting Information).

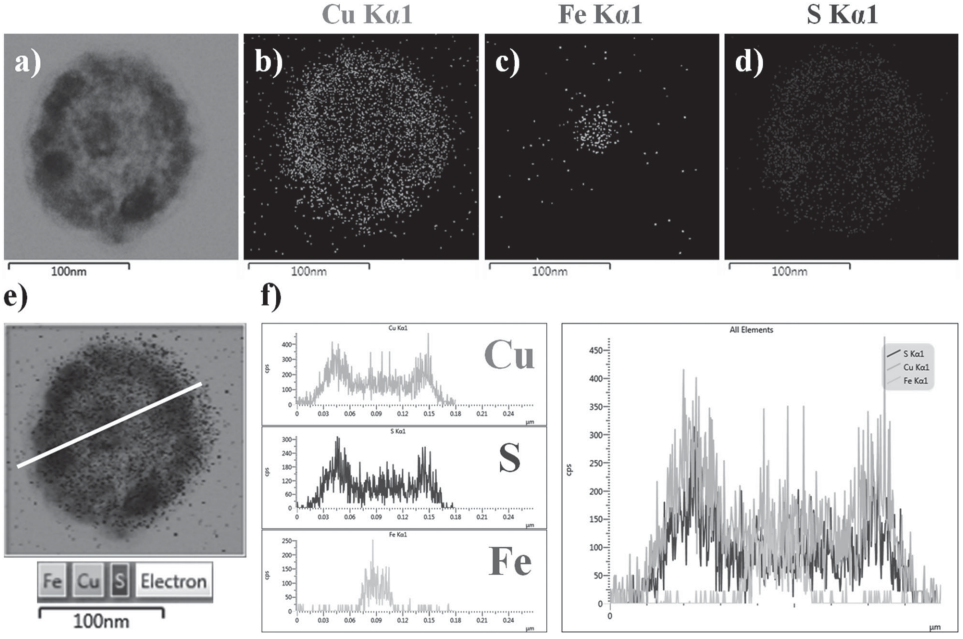

Figure 3. a) TEM image of the as-synthesized Fe_3O_4@CuS NPs and the elemental analysis of b) Cu, c) Fe, d) S, and e) the merged image. f) The corresponding EDS line scan profiles, where the white line indicates the path of electron beam for the line-scan in (e). The EDS analysis was captured on the nickel TEM grids.

2.2. Surface Modification of Fe_3O_4@CuS NPs

To further increase the biological compatibility of the Fe_3O_4@CuS NPs, we modified polyethylene glycol (PEG) available on their surfaces. Modifying PEG can increase the residence time of nanomaterials in blood circulation.[14] The method for preparing the Fe_3O_4@CuS-PEG NPs involved forming a copper–sulfur (Cu–S) bond[15] to modify MPA (3-mercaptopropionic acid) on the surface of the material and then forming an amide bond to modify PEG (Scheme 1) on the surface; hence, a positively charged amino functional group (NH_2) was exposed on the surface of NPs. Because cell membranes have negatively charged surfaces, positively charged surfaces increase the likelihood of NPs being ingested into the cancer cells. Figure S7a,b of the Supporting Information depicts the TEM images of the Fe_3O_4@CuS NPs with modified MPA and PEG on their surfaces. Modifying MPA and PEG does not affect the morphology of NPs. DLS was used to measure the Zeta potential and hydrodynamic diameter after each modification procedure (Figure S8, Supporting Information). The surface charge of Fe_3O_4@CuS was −2.41 mV; however, its surface was negatively charged such that its potential became −26.7 mV because of the exposure of the carboxyl functional group after the modification of MPA. Subsequently, the potential changed from negative to positive (+16.4 mV) after the PEG modification, resulting in the exposure of the amino functional group on the surface. The hydrodynamic diameter of Fe_3O_4@CuS was 152.5 nm, which is greater than the average particle size observed in the TEM images because PVP used in the synthesis process covered the surface. However, the hydrodynamic diameter decreased to 140.3 nm after the MPA modification, and this reduction in diameter was attributable to ethanol; this is because the MPA modification procedure was conducted in ethanol. To prove that ethanol induced the removal of PVP from the surface of the material, we placed Fe_3O_4@CuS in an ethanol solution and stirred the colloidal solutions for 12 h (Figure S8c, Supporting Information). The surface potential of Fe_3O_4@CuS changed from −2.41 to −17.1 mV because the sulfur ions (S^{2-}) were exposed on the CuS shell. Moreover, the hydrodynamic diameter decreased from 152.5 to 140.1 nm. This suggests that ethanol induced the removal of PVP from the surface. The removal of PVP also enables MPA to be attached onto the surface of NPs smoothly. After the PEG modification process, the hydrodynamic diameter increased to 146.9 nm again. This signifies that PEG was successfully modified on the surface of the material. Although Fourier transform infrared spectroscopy (FT-IR) is the optimal technique for confirming the modification of PEG on the surface, an strong absorption was observed at NIR for Fe_3O_4@CuS-PEG; hence, obtaining a high-quality FT-IR spectrum was difficult. Therefore, to prove that PEG was successfully conjugated onto the surface of NPs using a fluorescence technique, fluorescein isothiocyanate (FITC) was conjugated onto the surface through isothiourea bond formation because of the spontaneous reaction of the amino group (NH_2) and isothiocyanate (NCS). Figure S9a of the Supporting Information shows that the fluorescence intensity of the FITC supernatants decreased compared with that of the initial FITC solution, and Figure S9b,c of the Supporting Information indicates the existence of a green fluorescent signal on the fluorescent image obtained after conjugating the surface of the material with FITC. However, no fluorescent signal was observed for the NPs without FITC conjugation. This thus confirms the modification of PEG on the surface of Fe_3O_4@CuS. To understand the stability of the synthesized Fe_3O_4@CuS-PEG NPs, the NPs having a copper ion concentration of 300 ppm were separately placed in 300 µL of water, PBS with a pH of 5.0, PBS with a pH of 7.0, 10% fetal bovine serum (FBS) and cell culture Dulbecco's Modified Eagle Medium (DMEM); these mixtures were observed after 7 d. PBS with a pH of 5.0 was used to emulate the endosomal and lysosomal environment in the cells, and PBS with a pH of 7.0 was used to emulate the environment outside the cells. As illustrated in Figure S10 in the Supporting Information, the morphology of the Fe_3O_4@CuS-PEG NPs did not change after placing them in the various solutions for 7 d, indicating that they exhibit extremely high structural stability. The surface area and pore diameter of the Fe_3O_4@CuS-PEG NPs was 41.4 $m^2\ g^{-1}$ and 10 nm, respectively, as observed using the Brunauer–Emmett–Teller method, indicating that the CuS shell of the Fe_3O_4@CuS-PEG NPs is a mesoporous structure (Figure S11, Supporting Information). A band with peak appeared around 62 nm attributed to the hollow cavity of CuS. A superconducting quantum interference device was used to measure the magnetisms of aqueous-phase Fe_3O_4 and Fe_3O_4@CuS-PEG NPs (Figure S12, Supporting Information). The saturation magnetizations (M_S) of Fe_3O_4 and Fe_3O_4@CuS-PEG were 96.3 and 89.9 emu g^{-1}, respectively. This shows that the hollow porous CuS shell did not significantly influence the magnetism. The inset figure shows a magnified portion of Figure S12 in the Supporting Information, and it indicates that both Fe_3O_4 and Fe_3O_4@CuS-PEG NPs have ferromagnetic property because the synthesized Fe_3O_4 NPs contain iron. The remnant magnetizations (B_R) of Fe_3O_4 and Fe_3O_4@CuS-PEG were 9.5 and 8.9 emu g^{-1}, respectively, and their coercivities (H_C) were 50.1 and 45.7 Oe, respectively.

2.3. UV–vis–NIR Spectra of Fe_3O_4@CuS NPs

Figure 4a shows the UV–vis–NIR absorption spectra for the Fe_3O_4, Fe_3O_4@Cu_2O, Fe_3O_4@CuS, and Fe_3O_4@CuS-PEG NPs dispersed in water. The aqueous-phase Fe_3O_4 did not exhibit the characteristic absorption peak. After the cuprous oxide shell was coated onto the surfaces of the NPs, the absorption bands appeared in the positions less than 500 nm because of the contribution of cuprous oxide. According to theoretical calculations conducted from the Mie scattering theory by Wang et al.,[11,16] dipole (350 nm), quadrupole (290 nm), and octupole (230 nm) scattering peaks are located from right to left on the UV spectrum for the cuprous oxide structure. Moreover, an NIR absorption band with a broad absorption range (650–1300 nm) was generated resulting from the CuS shell contribution after the formation of Fe_3O_4@CuS, while the absorption less than 500 nm was attributable to the absorption of the CuS band gap.[5b,5c,17] The UV–vis–NIR absorption behavior did not change after the PEG modification on the surface of Fe_3O_4@CuS. The absorption of the synthesized Fe_3O_4@CuS-PEG NPs at NIR covered both ranges of 650–950 nm for the first NIR biological window and 1000–1350 nm for the

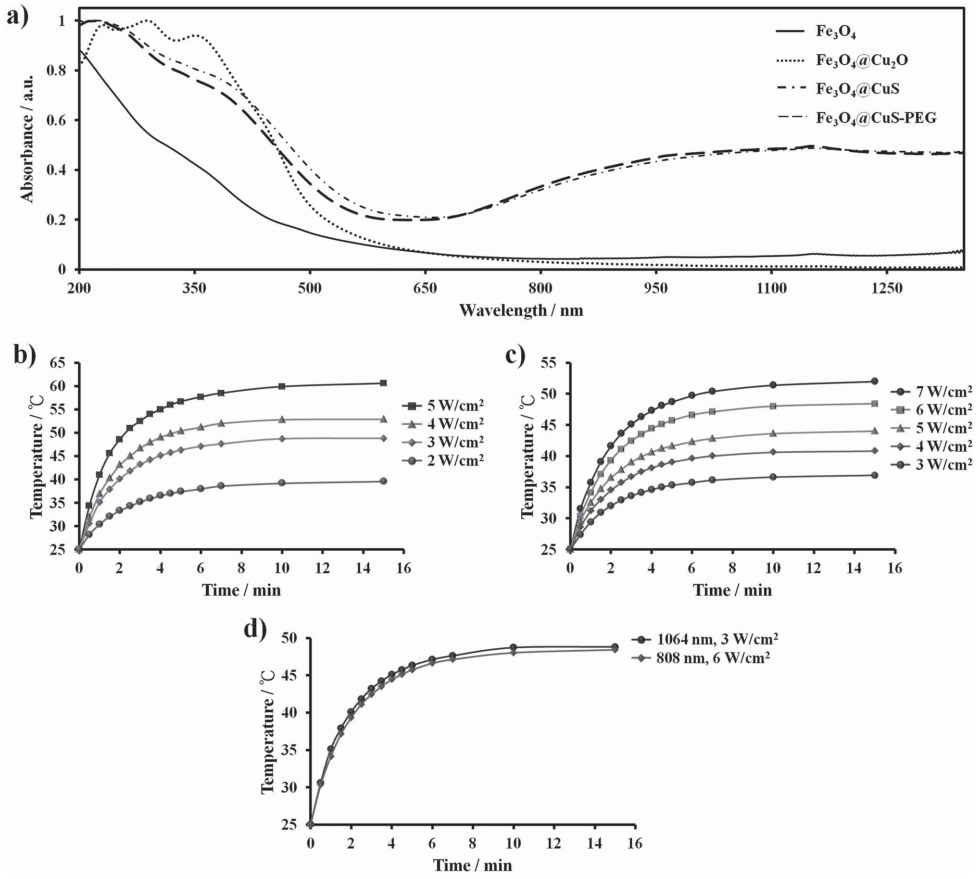

Figure 4. a) UV–vis–NIR absorption spectra of the Fe_3O_4, Fe_3O_4@Cu_2O, Fe_3O_4@CuS, and Fe_3O_4@CuS-PEG colloidal solutions. Temperature elevation profiles of Fe_3O_4@CuS-PEG solutions with Cu ion concentrations at 300 ppm under b) 1064 nm and c) 808 nm diode laser irradiation at different power intensities. d) Photothermal heating curves of Fe_3O_4@CuS-PEG solutions with Cu ion concentration at 300 ppm under 1064 nm laser irradiation at the power of 3 W cm^{-2} and 808 nm laser irradiation at the power of 6 W cm^{-2}.

second NIR biological window.[4a] Therefore, 808 and 1064 nm NIR laser irradiation can be potentially used for photothermal therapy. Considering the hollow structure of CuS nanoparticle, we have taken the average diameter, the shell thickness, and the density (4.76 g cm^{-3}) together to estimate molar extinction coefficients at 808 and 1064 nm. According to Beer's law, the ε values are 3.5×10^{10} cm^{-1} M^{-1} at 808 nm and 4.9×10^{10} cm^{-1} M^{-1} at 1064 nm. The better photothermal therapy is expected if 1064 nm NIR laser is used for Fe_3O_4@CuS-PEG. Furthermore, the molar extinction coefficient of our material at 1064 nm was higher than the value reported previously (2.6×10^7 cm^{-1} M^{-1}).[18] This indicates that the synthesized Fe_3O_4@CuS-PEG NPs are superior for applications for photothermal therapy in the second NIR biological window.

2.4. Response to Laser Ablation for Colloidal Solutions

Because the Fe_3O_4@CuS-PEG NPs exhibited a strong absorption in the NIR region, we conducted a comparison to reveal the efficacy in the photothermal heating observed at wavelengths between 1064 and 808 nm. However, both light intensity (W cm^{-2}) and beam size are vital variables for comparing photothermal effects, particularly in tumor photothermal therapy for animals. This is because the coverage of irradiation tumors and the amount of irradiated NPs are determined according to the beam size. The beam size of the 1064 nm laser we used was 0.05 cm^2 and that of the 808 nm laser was 0.16 cm^2. To ensure a reasonable comparison of the 808 and 1064 nm lasers, we reduced the beam size of the 808 nm laser to approximately 0.05 cm^2. In the heating curve tests conducted for evaluating photothermal conversion, the Fe_3O_4@CuS-PEG solutions were irradiated using the NIR lasers (Figure 4b–d and Figure S13, Supporting Information), and the temperature of the Fe_3O_4@CuS-PEG solutions increased with the 808 nm and 1064 nm laser irradiation as increased material dosage and irradiation power. According to the change in irradiation power (Figure 4b,c) or material dosage (Figure S13, Supporting Information), the heating efficiency observed at an irradiation wavelength of 1064 nm was superior to that of 808 nm. This result is consistent with our obervation where the absorption coefficient observed at the 1064 nm wavelength (4.9×10^{10} cm^{-1} M^{-1}) was superior to that obtained at the 808 nm wavelength (3.5×10^{10} cm^{-1} M^{-1}). The water without the NPs reached only 27 °C after 15 min of irradiation. When we maintained the copper ion concentration at 300 ppm for comparing the 808 and 1064 nm wavelengths, the irradiation intensity for 808 nm must be increased to 6 W cm^{-2} to ensure a comparable heating

effect at 1064 nm, with an irradiation of 3 W cm^{-2}. Subsequently, the photothermal conversion efficiency was quantified following the method developed by Roper et al.[19] The temperature of the colloidal solution was recorded upon 808 or 1064 nm illumination until reaching a steady state temperature, followed by an operation to shut off laser giving solution cooling process (Figure S14, Supporting Information). The heat conversion efficiency was calsulated to be 15.7% at 808 nm and 19.2% at 1064 nm. Furthermore, according to Lu and coworkers,[20] the structure of the synthesized hollow-structured CuS NPs presented a collapse phenomenon after the 900 nm laser irradiation at 2.0 W cm^{-2} for 40 s. Therefore, after the synthesized Fe_3O_4@CuS-PEG NP was irradiated with 1064 nm at 3 W cm^{-2} for 15 min, the structure did not collapse, as observed in the TEM image (Figure S15, Supporting Information).

2.5. Biocompatibility Subjected to MTT Assay

Before the in vitro photothermal therapy experiments, MTT assay was used for examining cytotoxicity to identify the biological compatibility of the Fe_3O_4@CuS-PEG NPs. We used a HeLa cell line (human cervical cancer cell line) as a model. We treated the cells with the Fe_3O_4@CuS-PEG NPs at copper concentrations of 0, 25, 50, 100, 200, 300, 400, or 500 ppm and incubated the cells for 24 h at 37 °C. We observed that the survival rate of the HeLa cells was maintained at more than 90%, even after the copper ion concentration reached 500 ppm, with no significant cytotoxicity (Figure S16, Supporting Information). Hence, the Fe_3O_4@CuS-PEG NPs possess high biological compatibility. Because the Fe_3O_4@CuS-PEG NPs contain iron oxide, an external magnet may be added to increase the material dosage accumulation within the cells through magnetic attraction. Therefore, we incubated 300 ppm of Fe_3O_4@CuS-PEG NPs with the HeLa cells with (magnetic attraction for 2 h) and without magnetic attraction (incubation for the same 2 h) and used ICP-AES to quantify the copper ion concentration ingested by the cells. Only 22% of the copper ion concentration was ingested by the cells without magnetic attraction, whereas the concentration increased to 65% for the group containing the cells having magnetic attraction. Therefore, the material dosage ingested by cells may increase through magnetic attraction induced by an external magnet. For the subsequent in vitro photothermal therapy experiments, irradiations of 808 and 1064 nm under magnetic and nonmagnetic attractions were observed.

2.6. In Vitro Performance upon NIR Lasers Exposure

Figure 5a shows a fluorescent image indicating the effect of cancer cells poisoning observed in in vitro photothermal therapy. For cells fed with the Fe_3O_4@CuS-PEG NPs without laser irradiation, no effective cell damage effect was observed. This result is consistent with that of the aforementioned cytotoxicity test. For the group subjected to the 1064 nm irradiation,

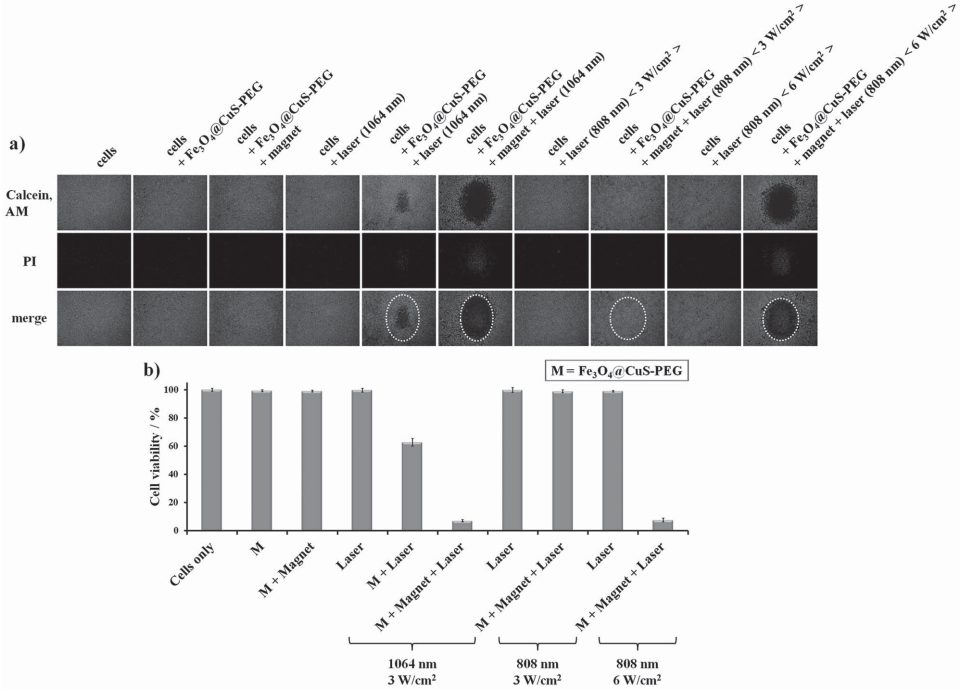

Figure 5. In vitro photothermal efficacy for HeLa cells alone, HeLa cells with Fe_3O_4@CuS-PEG respectively with or without exposure of 1064 and 808 nm diode lasers for 10 min exposure. For the groups with magnet, the magnet was applied with 2 h of magnetic attraction, followed by 10 min of laser irradiation. a) Fluorescence images of live and dead cells with different treatments. Green fluorescence represents the live cells stained with Calcein, AM. Red fluorescence represents the dead cells stained with propidium iodide (PI). The white dotted circles indicate the laser beam spot. b) Cell viability determined from the integrated intensity of the Calcein, AM fluorescence enclosed in the laser beam spot (MFe_3O_4@CuS-PEG). The laser beam spot has been restricted to be ≈0.05 cm^2 for both 1064 and 808 nm lasers.

the cells did not die when they were not fed with the NPs. However, when the cells were fed with the material followed by 1064 nm irradiation, a propidium iodide (PI) fluorescent signal appeared within the beam size range in the fluorescent image view. This identifies that the cells died after the Fe_3O_4@CuS-PEG NPs were subjected to the 1064 nm laser irradiation at 3 W cm^{-2} for 10 min. The fluorescent image indicates that when magnetic attraction was included followed by 1064 nm irradiation, the number of killed HeLa cells significantly increased. For the 808 nm laser group, applying 3 or 6 W cm^{-2} irradiation without the feeding NPs did not result in cell death. Even when the cells were subjected to material feeding in addition to magnetic attraction followed by the 808 nm irradiation at 3 W cm^{-2}, no significant poisoning effect was observed. According to the heating curve shown in Figure 4c, the temperature reached only 35 °C under this condition, indicating a negligible effect of photothermal therapy. However, when the NPs were fed in addition to magnetic attraction followed the 808 nm irradiation at 6 W cm^{-2}, clear PI fluorescent signals were observed, indicating that the HeLa cells were killed. According to the results (Figure 5b), the cell survival rate decreased to 63% when the Fe_3O_4@CuS-PEG NPs were subjected to 1064 nm irradiation for 10 min; the cell survival rate further decreased to 7% when magnetic attraction was included before irradiating the cells. This is because magnetic attraction possibly increased the dosage of the material ingested by the cells, improving the photothermal therapy effect. This also proves that our NPs has potential applicability for magnetic targeting through the addition of a magnet. However, for the 808 nm experimental group, the cell survival rate was maintained at more than 95% under the condition of magnetic attraction and 3 W cm^{-2} irradiation. Nevertheless, with 6 W cm^{-2} of irradiation, the cell survival rate was significantly reduced to 7%, which is consistent with the result obtained using the 1064 nm irradiation at 3 W cm^{-2}. Therefore, at the same copper concentration of 300 ppm, the intensity of the 808 nm laser irradiation applied to the Fe_3O_4@CuS-PEG NPs must be increased twofold to obtain a photothermal therapy effect similar to that observed at the 1064 nm irradiation.

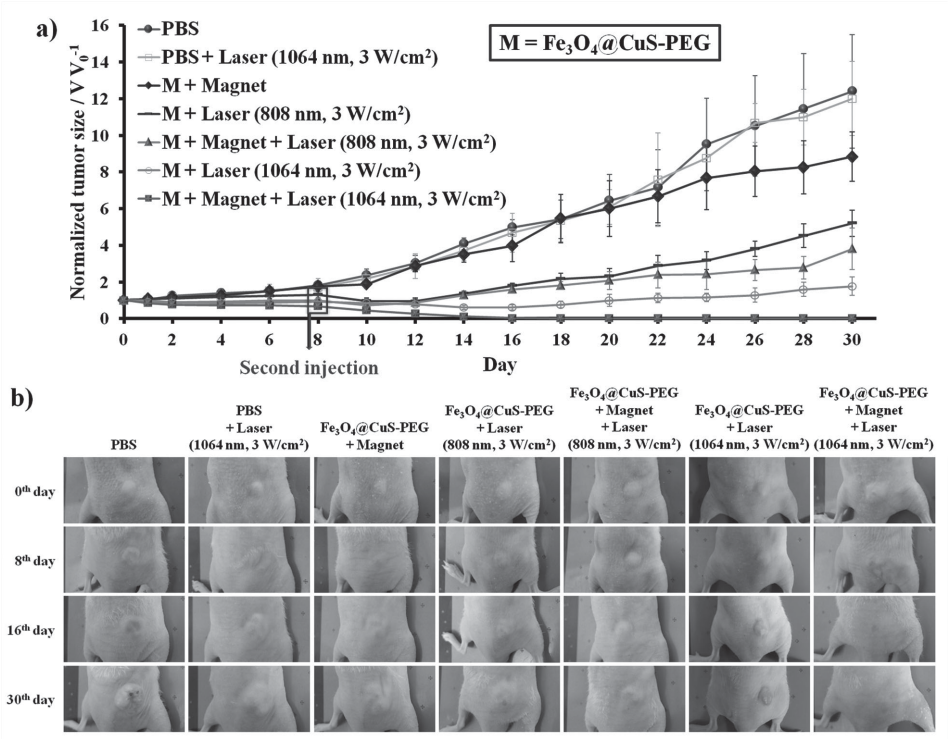

Figure 6. a) Tumor growth curves with different treatments ($n = 4$). b) The photographs of mice taken before and after treatments at different dates. NIR illumination was, respectively, performed using 1064 and 808 nm diode lasers for 30 min exposure at 3 W cm^{-2}. For the groups with magnet, the magnet was applied with 30 min of magnetic attraction, followed by the laser irradiation of 30 min.

2.7. In Vivo Studies in Photothermal Therapy, Toxicity, and MR Imaging

We conducted a subsequent in vivo photothermal therapy experiments. In this experiment, the laser power was fixed at 3 W cm^{-2} for comparing the tumor growth inhibition effect at the 808 and 1064 nm wavelengths. HeLa cells were injected into the backs of nude mice through subcutaneous injection, and 24 mice having tumors were randomly grouped into six groups. For the group involving material injection, we intravenously injected 20 mg kg^{-1} of Fe_3O_4@CuS-PEG NPs into the nude mice through the tail vein. Furthermore, regarding the group involving magnetic attraction, we injected the material into the mice; next, we conducted magnetic attraction 30 min by using an external magnet as well as uniform laser irradiation onto the tumor for 30 min. The beam size of the laser was fixed at 0.05 cm^2 that it cannot cover the entire tumor. Therefore, we arbitrarily selected three sites on the tumor and irradiated each site for 10 min. **Figure 6** shows that when only PBS was injected, for which a group with 1064 nm irradiation only and Fe_3O_4@CuS-PEG injection in addition to magnetic attraction without laser irradiation all existed, tumors increased with the number of observation days. Nevertheless, all groups subjected to material injection in addition to laser irradiation (Fe_3O_4@CuS-PEG + 1064 nm; Fe_3O_4@CuS-PEG + magnet + 808 nm; Fe_3O_4@CuS-PEG + magnet + 1064 nm) exhibited certain levels of tumor growth inhibition effects. In the first 8 d after laser irradiation, the difference in the tumor sizes of the mice in the three groups was not significant. The tumor sizes remained unchanged, without enlargement or shrinkage. Therefore, we injected the second dose on the 8th day and repeated the same operating modes: Fe_3O_4@CuS-PEG + 1064 nm; Fe_3O_4@CuS-PEG + magnet + 808 nm; and Fe_3O_4@CuS-PEG + magnet + 1064 nm. The results indicated that the tumors of the mice in

the Fe_3O_4@CuS-PEG + magnet + 1064 nm group were significantly inhibited and even completely disappeared on the 12th day, with no tumor recurrence up to the 30th day. Regarding the Fe_3O_4@CuS-PEG + 1064 nm and Fe_3O_4@CuS-PEG + magnet + 808 nm groups, the tumors could not be completely removed; however, a tumor growth inhibition capability was observed. Remarkably, compared with the Fe_3O_4@CuS-PEG + magnet + 808 nm group, the Fe_3O_4@CuS-PEG + 1064 nm group exhibited better inhibitory effect on tumors growth. In general, the tumors of the mice in the Fe_3O_4@CuS-PEG + magnet + 808 nm group enlarged slowly. The results indicated that tumors can be effectively removed at 1064 nm with facilitation of magnetic attraction. However, although the performance of 808 nm in photothermal ablation was not comparable to that of 1064 nm, a certain level of tumor growth inhibition was still observed.

Figure S17 of the Supporting Information shows the biodistribution after injection of Fe_3O_4@CuS-PEG NPs into mice bearing HeLa tumors through tail vein with or without 30 min of magnetic targeting. The tissues were surgically removed after 30 min, 7 d and 30 d of injection. Heart, liver, spleen, lung, kidneys, and tumor tissues were taken and subjected to ICP-AES analysis to determine quantitatively the contents of NPs in these tissues. In comparison, the amount of NPs accumulated at the tumor in the group with the magnetic attraction is larger than that observed in the tumors of the group without magnetic attraction after 30 min. The attraction of external magnetic field contributed to the accumulation of sufficient NPs in the tumor and thus improved the effect of subsequent treatments. Basically, the NPs were gradually eliminated as time prolonged from both nil- and with-magnet groups. According to the report of Lu and co-workers, PEGylated CuS NP was considered as biodegradable nanoparticles. In living animals, the elimination of CuS NPs in liver may majorly be attributed to Cu metabolism by the hepatocytes through hepatobiliary excretion within a month.[15a] The experiment for the biological toxicity examination involved intravenously injecting 20 mg kg^{-1} of the Fe_3O_4@CuS-PEG NPs into the nude mice with tumors through the tail vein. One group was subjected to magnetic attraction for 30 min, whereas the other group was not. The mice were sacrificed after 30 min, 7 d and 30 d, respectively, and their blood was used for blood biochemical analysis to examine liver (ALP, AST, ALT, and TBIL) and renal function (BUN, UA, and CRE) indices. The experimental results indicate that within the first 30 d, no difference existed between the experimental groups and control group subjected to PBS injection (Figure S18, Supporting Information). In addition, we resected and then dissected the organs of the heart, liver, spleen, lung, and kidney for histological analysis at 30 min, 7th day, and 30th day post-injection for any change in the morphology due to material toxicity (Figure S19, Supporting Information). Once again, one group was subjected to magnetic attraction for 30 min, whereas the other group was not. The tissues after hematoxyline and eosin staining showed well organized cell structure as that of the control set. Especially, the intact morphology of spleen, which play important role in blood purification do not show any change in morphology due to absence of immune activity. With these preliminary toxicological results, it is believed that the current NPs proposed have no acute toxicity as a cancer medicine.

Finally, because iron oxide NPs could be used as T_2 contrast agents for MRI, Fe_3O_4@CuS-PEG NPs were prepared in 1.3% agarose gel at various iron ion concentrations. A 9.4 T USR Preclinical MRI System for animals was used to measure r_2 values of the Fe_3O_4 and Fe_3O_4@CuS-PEG NPs and they were 314.37 and 302.02 mM^{-1} s^{-1}, respectively (**Figure 7**). The difference

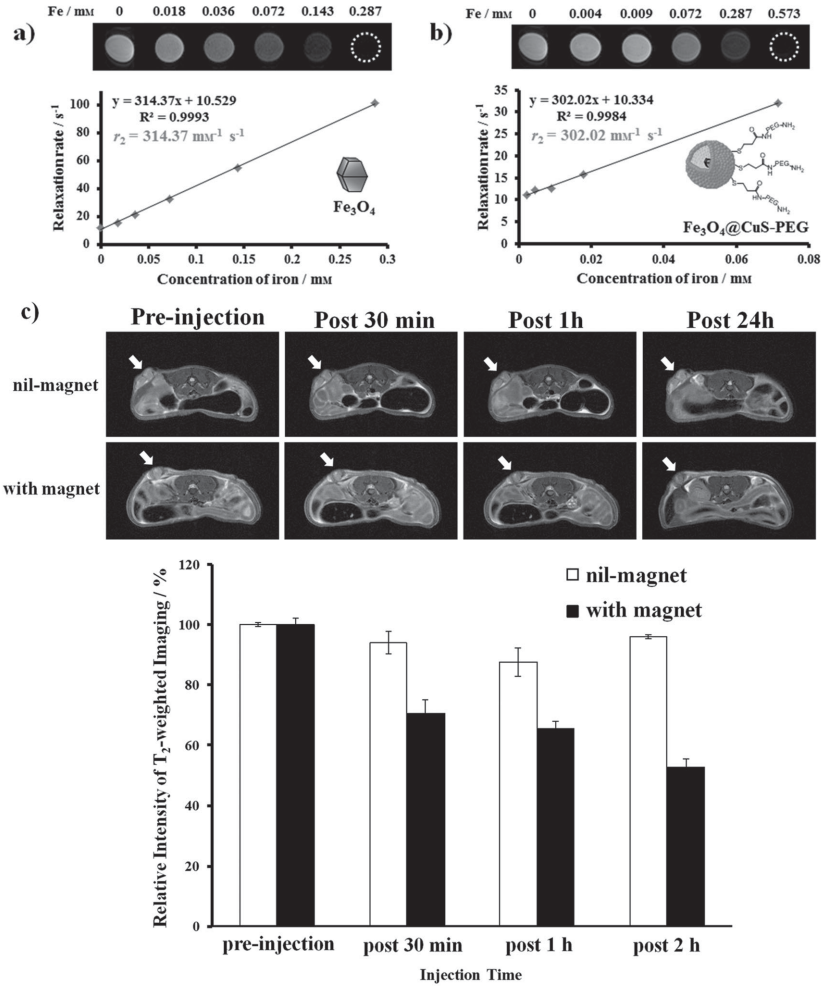

Figure 7. The r_2 values of a) Fe_3O_4, and b) Fe_3O_4@CuS-PEG NPs were calculated by T_2 relaxation (T_2^{-1} / s^{-1}) rate versus iron concentration. c) The T_2-weighted images of Fe_3O_4@CuS-PEG NPs were monitored using a 9.4 T animal microMRI system as the NPs were administrated by the intravenously injection at the dose of 20 mg kg^{-1}. The images were captured on the pre-injection and post-injection for 30 min, 1 h, and 24 h after particles administration. For the group with the magnetic attraction, the magnet was applied on the tumor site for 30 min after injection of NPs. White arrows indicate the location of tumor.

between the r_2 values of the Fe_3O_4 and Fe_3O_4@CuS-PEG NPs was not significant because the CuS was a hollow porous structure; hence, water molecules could have readily accessed the interior of CuS. The mice were injected with HeLa cells hypodermically. The experiments were conducted after 8 d of tumor growth, and the tumors then were subjected to the measurements using a 9.4 T animal micro MRI system. Fe_3O_4@CuS-PEG NPs were administrated by the intravenously injection at a dosage of 20 mg kg^{-1}. The external magnet was applied for 30 min after injection (without magnet as sham control). The contrast change in signal was monitored at pre-injection, 30 min, 1 h, and 24 h post-injection for MR images. The quantitative analysis showed the contrast decrease as time with the contrast signal of tumor after magnetic attraction reduced to 65% after 1 h (Figure 7c). Contrarily, the nil-magnet group in the tumor only displayed a slight drop with 88% in intensity after 1 h. This indicates that once the Fe_3O_4@CuS-PEG NPs was injected into mice's body, the manipulation by an external magnet caused the NPs to accumulate at the tumor in large quantity in a fairly short period of time, which significantly improved the negative contrast effect at the tumor. Apart from confirming that Fe_3O_4@CuS-PEG NPs is an effective MRI T_2 contrast agent, it also evidences that the NPs can be used as an effective magnetic target. It is noted that although MR image indicated greater NPs accumulation at post-1 h injection, the early stage in NPs accumulation (30 min) upon magnetic attraction has allowed us to readily discriminate in vivo phoththermal efficacy between 808 and 1064 nm laser irradiation.

3. Conclusion

We have fabricated an effective NIR responsive rattle-type Fe_3O_4@CuS nanoparticles that display broad NIR absorption covering 1st and 2nd biological windows. The 1064 nm reveals higher absorption coefficient than that of 808 nm. Consequently, twofold larger in laser intensity was needed for 808 nm relative to for 1064 nm in order to exhibit the same efficacy for cancer cells damage in vitro. However, both 808 and 1064 nm irradiation display the capability to control tumor size in growth. Although 808 nm cannot completely remove tumor, the tumor growth can be inhibited in a certain degree. Perhaps, the multiple dosing in particle and laser exposure is necessary when using 808 nm. On the other hand, the 1064 nm with larger absorption coefficient and better tissue penetration has shown promising results to completely eliminate tumor. Because of the presence of the magnetic Fe_3O_4, the multifunctional rattle-type Fe_3O_4@CuS features magnetic guidance, photothermal ablation and diagnosis providing a potent therapeutic choice in the biomedical field.

Supporting Information

Supporting Information is available from the Wiley Online Library or from the author.

Acknowledgements

The authors appreciate the financial support from the Ministry of Science and Technology (MOST 103–2113-M-006–008-MY2), and in part by the Headquarters of University Advancement at the National Cheng Kung University, which is sponsored by the Ministry of Education, Taiwan, ROC. All animal treatments and surgical procedures were performed in accordance with the guidelines of National Cheng Kung University (NCKU) Laboratory Animal Center (Tainan, Taiwan). All animals received humane care in compliance with NCKU guidelines for the maintenance and use of laboratory animals in research. All of the experimental protocols involving live animals were reviewed and approved by the Animal Experimentation Committee of NCKU.

Received: July 21, 2015
Revised: August 20, 2015
Published online: September 24, 2015

[1] E. J. Silvester, F. Grieser, B. A. Sexton, T. W. Healy, *Langmuir* **1991**, *7*, 2917.
[2] a) Y. Xie, L. Carbone, C. Nobile, V. Grillo, S. D'Agostino, F. Della Sala, C. Giannini, D. Altamura, C. Oelsner, C. Kryschi, P. D. Cozzoli, *ACS Nano* **2013**, *7*, 7352; b) S. W. Hsu, C. Ngo, A. R. Tao, *Nano Lett.* **2014**, *14*, 2372; c) M. Liu, X. Xue, C. Ghosh, X. Liu, Y. Liu, E. P. Furlani, M. T. Swihart, P. N. Prasad, *Chem. Mater.* **2015**, *27*, 2584.
[3] a) J. Pérez-Juste, I. Pastoriza-Santos, L. M. Liz-Marzán, P. Mulvaney, *Coord. Chem. Rev.* **2005**, *249*, 1870; b) S. K. Kang, Y. Kim, M. S. Hahn, I. Choi, J. Lee, J. Yi, *Curr. Appl. Phys.* **2006**, *6S1*, e114.
[4] a) A. M. Smith, M. C. Mancini, S. Nie, *Nat. Nanotechnol.* **2009**, *4*, 710; b) K. Welsher, S. P. Sherlock, H. Dai, *Proc. Natl. Acad. Sci. USA* **2011**, *108*, 8943.
[5] a) M. Zhou, R. Zhang, M. Huang, W. Lu, S. Song, M. P. Melancon, M. Tian, D. Liang, C. Li, *J. Am. Chem. Soc.* **2010**, *132*, 15351; b) Y. Li, W. Lu, Q. Huang, M. Huang, C. Li, W. Chen, *Nanomedicine* **2010**, *5*, 1161; c) Q. Tian, M. Tang, Y. Sun, R. Zou, Z. Chen, M. Zhu, S. Yang, J. Wang, J. Wang, J. Hu, *Adv. Mater.* **2011**, *23*, 3542; d) K. Dong, Z. Liu, Z. Li, J. Ren, X. Qu, *Adv. Mater.* **2013**, *25*, 4452; e) Z. Zha, S. Zhang, Z. Deng, Y. Li, C. Li, Z. Dai, *Chem. Commun.* **2013**, *49*, 3455.
[6] a) Q. Zhan, J. Qian, H. Liang, G. Somesfalean, D. Wang, S. He, Z. Zhang, S. Andersson-Engels, *ACS Nano* **2011**, *5*, 3744; b) Y. F. Wang, G. Y. Liu, L. D. Sun, J. W. Xiao, J. C. Zhou, C. H. Yan, *ACS Nano* **2013**, *7*, 7200.
[7] a) Q. Tian, F. Jiang, R. Zou, Q. Liu, Z. Chen, M. Zhu, S. Yang, J. Wang, J. Wang, J. Hu, *ACS Nano* **2011**, *5*, 9761; b) Q. Tian, J. Hu, Y. Zhu, R. Zou, Z. Chen, S. Yang, R. Li, Q. Su, Y. Han, X. Liu, *J. Am. Chem. Soc.* **2013**, *135*, 8571; c) Q. Xiao, X. Zhang, W. Bu, W. Ge, S. Zhang, F. Chen, H. Xing, Q. Ren, W. Fan, K. Zhao, Y. Hua, J. Shi, *J. Am. Chem. Soc.* **2013**, *135*, 13041; d) J. Mou, P. Li, C. Liu, H. Xu, L. Song, J. Wang, K. Zhang, Y. Chen, J. Shi, H. Chen, *Small* **2015**, *11*, 2275; e) S. Wang, A. Riedinger, H. Li, C. Fu, H. Liu, L. Li, T. Liu, L. Tan, M. J. Barthel, G. Pugliese, F. De Donato, M. Scotto D'Abbusco, X. Meng, L. Manna, H. Meng, T. Pellegrino, *ACS Nano* **2015**, *9*, 1788; f) G. Yang, R. Lv, F. He, F. Qu, S. Gai, S. Du, Z. Wei, P. Yang, *Nanoscale* **2015**, *7*, 13747; g) L. Wu, M. Wu, Y. Zeng, D. Zhang, A. Zheng, X. Liu, J. Liu, *Nanotechnology* **2015**, *26*, 025102.
[8] C. C. Huang, K. Y. Chuang, C. P. Chou, M. T. Wu, H. S. Sheu, D. B. Shieh, C. Y. Tsai, C. H. Su, H. Y. Lei, C. S. Yeh, *J. Mater. Chem.* **2011**, *21*, 7472.
[9] R. K. Zheng, H. Gu, B. Xu, K. K. Fung, X. X. Zhang, S. P. Ringer, *Adv. Mater.* **2006**, *18*, 2418.
[10] M. Pang, H. C. Zeng, *Langmuir* **2010**, *26*, 5963.
[11] L. Zhang, H. Wang, *ACS Nano* **2011**, *5*, 3257.
[12] D. F. Zhang, H. Zhang, L. Guo, K. Zheng, X. D. Han, Z. Zhang, *J. Mater. Chem.* **2009**, *19*, 5220.

[13] a) J. Nai, Y. Tian, X. Guan, L. Guo, *J. Am. Chem. Soc.* **2013**, *135*, 16082; b) G. L. Miessler, D. A. Tarr, *Inorganic Chemistry*, Pearson/Prentice Hall, Upper Saddle River, NJ, USA **2011**.

[14] a) M. F. Tsai, S. H. Chang, F. Y. Cheng, V. Shanmugam, Y. S. Cheng, C. H. Su, C. S. Yeh, *ACS Nano* **2013**, *7*, 5330; b) Y. Liu, W. Wang, J. Yang, C. Zhou, J. Sun, *Asian J. Pharm. Sci.* **2013**, *8*, 159; c) Y. Zhang, N. Kohler, M. Zhang, *Biomaterials* **2002**, *23*, 1553.

[15] a) L. Guo, I. Panderi, D. D. Yan, K. Szulak, Y. Li, Y. T. Chen, H. Ma, D. B. Niesen, N. Seeram, A. Ahmed, B. Yan, D. Pantazatos, W. Lu, *ACS Nano* **2013**, *7*, 8780; b) Q. Xiao, X. Zheng, W. Bu, W. Ge, S. Zhang, F. Chen, H. Xing, Q. Ren, W. Fan, K. Zhao, Y. Hua, J. Shi, *J. Am. Chem. Soc.* **2013**, *135*, 13041.

[16] L. Zhang, D. A. Blom, H. Wang, *Chem. Mater.* **2011**, *23*, 4587.

[17] a) B. Li, Q. Wang, R. Zou, X. Liu, K. Xu, W. Li, J. Hu, *Nanoscale* **2014**, *6*, 3274; b) Y. Zhao, H. Pan, Y. Lou, X. Qiu, J. Zhu, C. Burda, *J. Am. Chem. Soc.* **2009**, *131*, 4253.

[18] G. Ku, M. Zhou, S. Song, Q. Huang, J. Hazle, C. Li, *ACS Nano* **2012**, *6*, 7489.

[19] D. K. Roper, W. Ahn, M. Hoepfner, *J. Phys. Chem. C* **2007**, *111*, 3636.

[20] L. Guo, D. D. Yan, D. Yang, Y. Li, X. Wang, O. Zalewski, B. Yan, W. Lu, *ACS Nano* **2014**, *8*, 5670.